CrossMark

Effect of aging treatment on mechanical properties and fracture behavior of friction stir processed Mg–Y–Nd alloy

Genghua Cao[1], Datong Zhang[1,*], Xicai Luo[1], Weiwen Zhang[1], and Wen Zhang[1]

[1] National Engineering Research Center of Near–Net Shape Forming for Metallic Materials, South China University of Technology, Guangzhou 510640, People's Republic of China

ABSTRACT

In this study, precipitation behavior of Mg–Y–Nd cast alloy during friction stir processing (FSP), and the effect of subsequent artificial aging on mechanical properties and fracture behavior of the FSP alloy were investigated. It is found that the coarse α-Mg grains and large second phases are greatly refined after FSP. Moreover, due to the heat input during processing and the natural cooling, β' and β_1 precipitates are also observed in the FSP alloy. The FSP specimens were subjected to subsequent artificial aging treatment, and the peak hardness is obtained at 150 °C for 54 h and 180 °C for 30 h. Strengths of the peak–aged specimens are further increased, which is attributed to the large quantity of β'' and β_1 precipitates, respectively. Meanwhile, elongations of the peak-aged specimens are both decreased. Due to the comprehensive effects of banded structures and fine grains, failure mechanisms of FSP and peak-aged specimens are all mixed ductile–brittle fracture mode. However, compared to the FSP specimens, different fracture paths are exhibited in peak–aged specimens.

Introduction

Friction stir processing (FSP) is a new processing technique for microstructure modification based on the basic principles of friction stir welding (FSW). In the past 15 years, FSP has been demonstrated effective in fabricating fine-grained structure and surface composites for the application of metal materials, and it can also be used to synthesize metal matrix composites and intermetallic compounds [1–8]. As a severe plastic deformation (SPD) technique, FSP generates high-temperature exposure and intense plastic deformation during processing, resulting in a complicated microstructure evolution, such as precipitates dissolution and coarsening, recrystallization process and texture formation. For age-hardenable alloys, the precipitation behavior during FSW/FSP is of great importance to achieve optimum mechanical properties. Fonda et al. [9] reported that the original precipitates in 2195 Al alloy were coarsened and dissolved during FSW, and were then replaced by different precipitates during cooling. Sato et al. [10] investigated

🖄 Springer

the microstructure evolution of 6063 Al during FSW, and different precipitation sequences were found in various regions of the weld since the thermal history strongly influenced the precipitate distribution. Verification of precipitation behavior is helpful for developing new FSP materials through the microstructure design approach. However, the precipitation behaviors during FSW or FSP are not investigated in detail in magnesium (Mg) alloys until present.

As precipitation strengthened Mg alloys, Mg–Y–Nd alloys have high strengths at room temperature with the aid of optimal heat treatment [11]. Su et al. [12] reported that strengths of Mg–4Y–2.4Nd–0.2Zn–0.4Zr casting (wt%) could be remarkably increased after solution treatment and subsequent aging, while the elongations are still low (about 5 %) due to the coarse grains. Kumar et al. [7, 13] selected the hot-rolled WE43 alloy as base metal (BM); the combination of FSP and aging improved the comprehensive mechanical properties of WE43 alloy, indicating grain refinement and precipitation behavior control can be used together to improve the mechanical properties of Mg–Y–Nd alloys. Conducting FSP on as-cast WE43 alloy, we found that the tensile strength of the FSP specimen (∼290 MPa) is close to Kumar's research, which is mainly attributed to the strong grain refinement effect of FSP [14]. However, since the original microstructures are quite different, especially the sizes of the α-Mg grains and the second phases, microstructure evolution mechanisms of the as–cast alloy during FSP may be different from that of the hot-rolled alloy.

As a multiple-phase Mg alloy, it is reported that five kinds of precipitates are formed in Mg–Y–Nd alloy during heat treatment, and the precipitation sequence is designated as follows: supersaturated solid solution (SSSS) → ordered Guinier–Preston zones (Zig–Zag shape) → β″ (D019 crystal structure) → β′ (base-centered orthorhombic structure) → β₁ (face-centered cubic structure) → β (face-centered cubic structure), which depends on the aging temperature and time [15–22]. In recent work, Nie et al. found that β″ precipitates were not detected in binary Mg–Nd alloy when aged at low temperatures, because the driving force in dilute Mg–RE alloys was too low to provide enough energy for the formation and growth of β″ precipitates [23]. Choudhuri et al. also reported that the Nd-rich clusters in Mg–Nd alloy were GP zones rather than β″ precipitates [24]. These studies indicate that the precipitation sequence in Mg–Y–Nd alloy is

relatively complicated. Since large deformation is introduced into the material at high temperature and high strain rate during FSP, the precipitation behavior of Mg–Y–Nd cast alloys under such complicated conditions has not been fully understood.

In this study, a Mg–Y–Nd casting with the compositions of Mg–4.27Y–2.94Nd–0.51Zr (wt%) was selected as BM. One of the works in this study is to investigate the precipitation behavior of Mg–Y–Nd cast alloy during FSP. Moreover, the other work is focussed on the effect of artificial aging on the FSP alloy, which aims to investigate the microstructure evolution after aging treatment and further improve the strengths of FSP specimens. The failure mechanisms of FSP and peak-aged specimens are also investigated.

Experimental

Mg–4.27Y–2.94Nd–0.51Zr (wt%) plates with a thickness of 6 mm were cut from cast billets and subjected to single-pass FSP at a rotation rate of 600 rpm and a traveling speed of 60 mm min⁻¹. A tool with a shoulder of 15 mm in diameter, a threaded conical pin of 4 mm in root diameter, and 5 mm in length was used. The tool tilt angle was 2.5°. Using the method as our previous work [25], K-type thermocouple with a diameter of 0.5 mm was inserted into the middle of the plates to measure the temperatures during FSP (Fig. 1). A Kistler CoMo injection–type device (Kistler Instrument AG, Winterthur, Switzerland) was used to continuously record the temperature history at a sampling rate of 0.25 s. After processing, the FSP specimens were subjected to artificial aging directly at 150 and 180 °C for the time from 1 to 72 h, respectively.

Microstructure observations were conducted by optical microscopy (OM), scanning electron microscopy (SEM), and transmission electron microscopy (TEM). The specimens for OM and SEM observation were cut perpendicular to the processing direction, and prepared by mechanical polishing then etching with a solution of 5 g picric acid + 10 ml acetic acid + 10 ml distilled water + 80 ml ethanol. Thin foils for TEM were ion-milled by a Gatan 691 miller at a voltage of 4 kV. The average grain size was measured by the mean linear intercept method. Second-phase particles analysis of the specimens was carried out by XRD with Cu Kα radiation.

Figure 1 Schematic diagram of temperature measurement.

Location of the thermocouple inserted
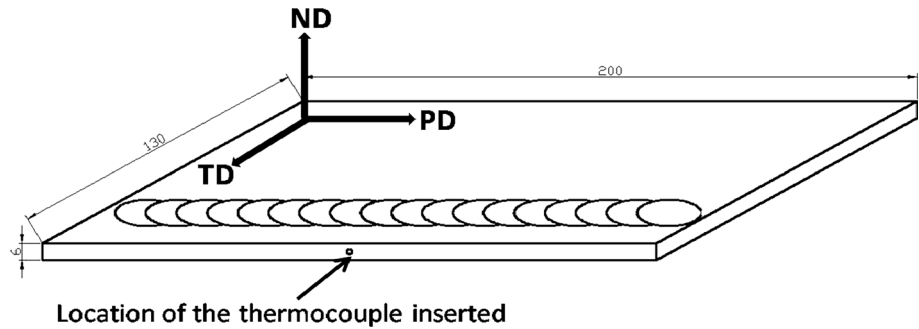
Vickers microhardness tests were measured by a hardness tester with a load of 0.98 N and a dwelling time of 10 s. Every indentation was measured three times and calculated the average value. Tensile specimens with a gauge length of 5 mm, a thickness of 1.5 mm, and a width of 3.5 mm were machined parallel to the processing direction with the gauge completely within the stirred zone (SZ). Tensile tests were performed on a SANS CMT5105 machine with a strain rate of $2 \times 10^{-3} \text{ s}^{-1}$. At least five specimens were tested to evaluate the average property values. Tensile fracture morphologies of TD (transverse direction, transverse to the processing direction) and PD (processing direction, parallel to the FSP direction) were subjected to SEM and OM examinations. The definition of the directions mentioned above is shown in Fig. 1.

Results

Microstructure evolution of Mg–Y–Nd cast alloy during FSP

Figure 2a shows the microstructure of BM specimen with coarse α-Mg grains ($\sim$53 μm). In addition, the coarse phases ($Mg_{12}Nd$) located at grain boundaries are shown in Fig. 2b [12, 26], and the small particles ($Mg_{24}Y_5$) are either individual or clustered in the intragranular region [26], as illustrated in the inserted image in Fig. 2b.

Figure 3a shows the surface appearance of the processed region. Due to the heat input by the friction effect between shoulder and work piece [2], the surface of FSP specimen is oxidized and turns dark. The cross section macrograph of FSP Mg–Y–Nd alloy is shown in Fig. 3b. A symmetrically basin-shaped SZ is

exhibited, and no obvious defects but onion-ring patterns can be seen clearly in SZ. Microstructure in the central region of SZ is shown in Fig. 3c, in which coarse-grained bands (CGB) and fine-grained bands (FGB) can be seen. The banded structure is examined by SEM and shown in Fig. 3d; the average grain size in SZ of FSP Mg–Y–Nd alloy is calculated as $\sim$2.7 μm. Figure 3e shows the back-scattered electron (BSE) image of particle–rich bands in SZ. It is reported that the temperature distribution will affect the microstructure homogeneity in SZ [27]. Furthermore, the material flow during FSP is complicated, which is significantly influenced by the tool design [2]. In this study, a threaded conical pin is used. Due to the stirring action, the materials transport during processing mainly includes the following two steps: (I) materials from advancing side to the retreating side; (II) materials from bottom to the top. During FSP, coarse second phases in BM are significantly broken into fine particles. Because of the different flow abilities between the second-phase particles and matrix, band structures are formed after processing. Other studies also proved that the formation of band structures is influenced by the dispersed particles, and particle-rich bands will cause significant grain refinement, which is attributed to its pinning effect during dynamic recrystallization (DRX) [28, 29]. On the other hand, DRX grains in particle-poor region are tended to be coarse.

The XRD patterns of BM and FSP specimens are shown in Fig. 4. It can be found that the dominated second phases in BM and FSP specimens are $Mg_{12}Nd$ and $Mg_{24}Y_5$. In addition, the corresponding diffraction peaks of second phases in FSP specimen are slightly weakened compared with BM (as shown by the rectangular marks in Fig. 4), indicating the dissolution behavior of the second phases during FSP.
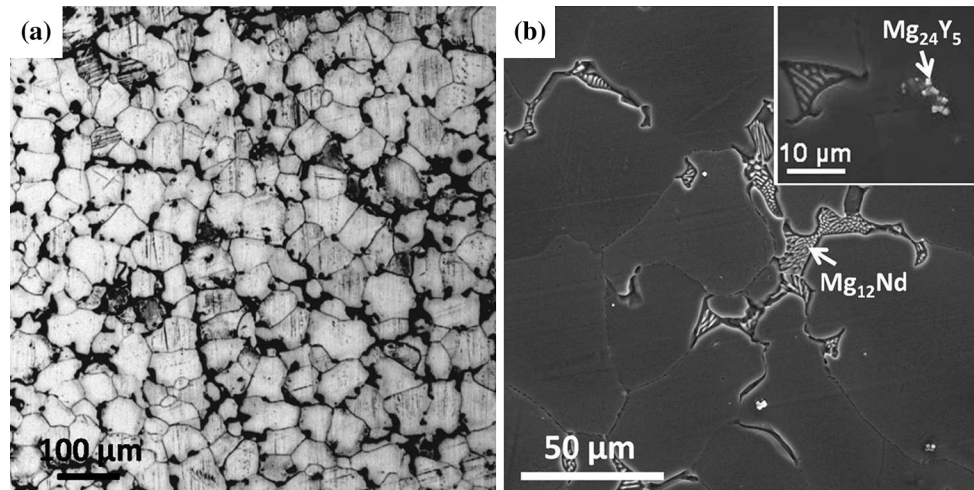
Figure 2 **a** OM and **b** SEM images of BM specimen.

After FSP, besides the small particles, quantities of precipitates can also be found in the intragranular region, and their distribution is quite uniform (Fig. 5a). It has been reported [15–19] that the precipitates found in Mg–Y–Nd alloys have the following characteristics: (i) The lamellar β'' precipitates ($Mg_3Y_{0.85}Nd_{0.15}$) with lattice parameters $a = 0.64$ nm and $c = 0.521$ nm, DO_{19} crystal structure, and their dimensions vary from 0.5 nm to 2 nm generally; (ii) The globular β' precipitates ($Mg_{12}YNd$ or $Mg_{24}Y_2Nd_3$) with lattice parameters $a = 0.64$ nm, $b = 2.223$ nm and $c = 0.521$ nm, base-centered orthorhombic structure, which has a diameter in the range of 4–30 nm generally; (iii) The plate-shaped β_1 precipitates ($Mg_{14}YNd_2$) with lattice parameters $a = 0.74$ nm, face-centered structure, which has a width ranging from 7 to 15 nm generally, and this phase is commonly in contact with β' precipitates at the two ends of the plates. As shown by the high-resolution electron microscopy (HREM) images in Fig. 5b, c, two kinds of precipitates are identified according to the different morphologies and structure analysis: (i) the globular β' precipitates with a dimension about 5 nm; (ii) the plate-shaped β_1 precipitates with a width of 4–11 nm. Figure 5b shows the selected area diffraction pattern (SADP) along the $[0001]_{Mg}$ orientation of the FSP specimen. Besides the matrix spots, the precipitate reflections appeared $1/4(1 - 100)_{Mg}$ between the matrix reflections are consistent with the presence of β' precipitates, with a base-centered orthorhombic structure ($a = 2a_{Mg} = 0.64$ nm, $b = 2.223$ nm and $c = c_{Mg} = 0.521$ nm). These features are in agreement with the previous works on Mg–RE alloys [15, 18–20].

The combined effect of FSP and aging on Mg–Y–Nd cast alloy

Mechanical properties of experimental specimens

Figure 6 shows the age hardening curves of the FSP specimens at 150 and 180 °C, respectively. The hardness of FSP specimen is measured as 94.6 VHN. When aged at 150 and 180 °C, the hardness curves are both increased first and then decreased. The peak-aged conditions are 150 °C × 54 h (106.4 VHN) and 180 °C × 30 h (109 VHN), respectively. Hereafter, these specimens are referred to FSP + 150 °C and FSP + 180 °C, respectively.

The results of tensile tests are summarized in Fig. 7 in the form of histograms. The ultimate tensile strength (UTS), yield strength (YS), and elongation of as-cast specimen are 199 MPa, 189 MPa and 5 %, respectively. After FSP, the strengths and elongation are significantly increased, which are mainly attributed to the microstructure modification by FSP [2]. According to the results mentioned above, four strengthening mechanisms are responsible for the strength improvement: (I) grain boundary strengthening from grain refinement, as observed by SEM (Fig. 3d); (II) dispersion strengthening from small particles, as examined by SEM (Fig. 3e); (III) solid solution strengthening from second-phase dissolution, as detected by XRD (Fig. 4); (IV) precipitation strengthening from precipitates, as observed by TEM (Fig. 5). In addition, grain refinement is the major reason for the ductility increasing.

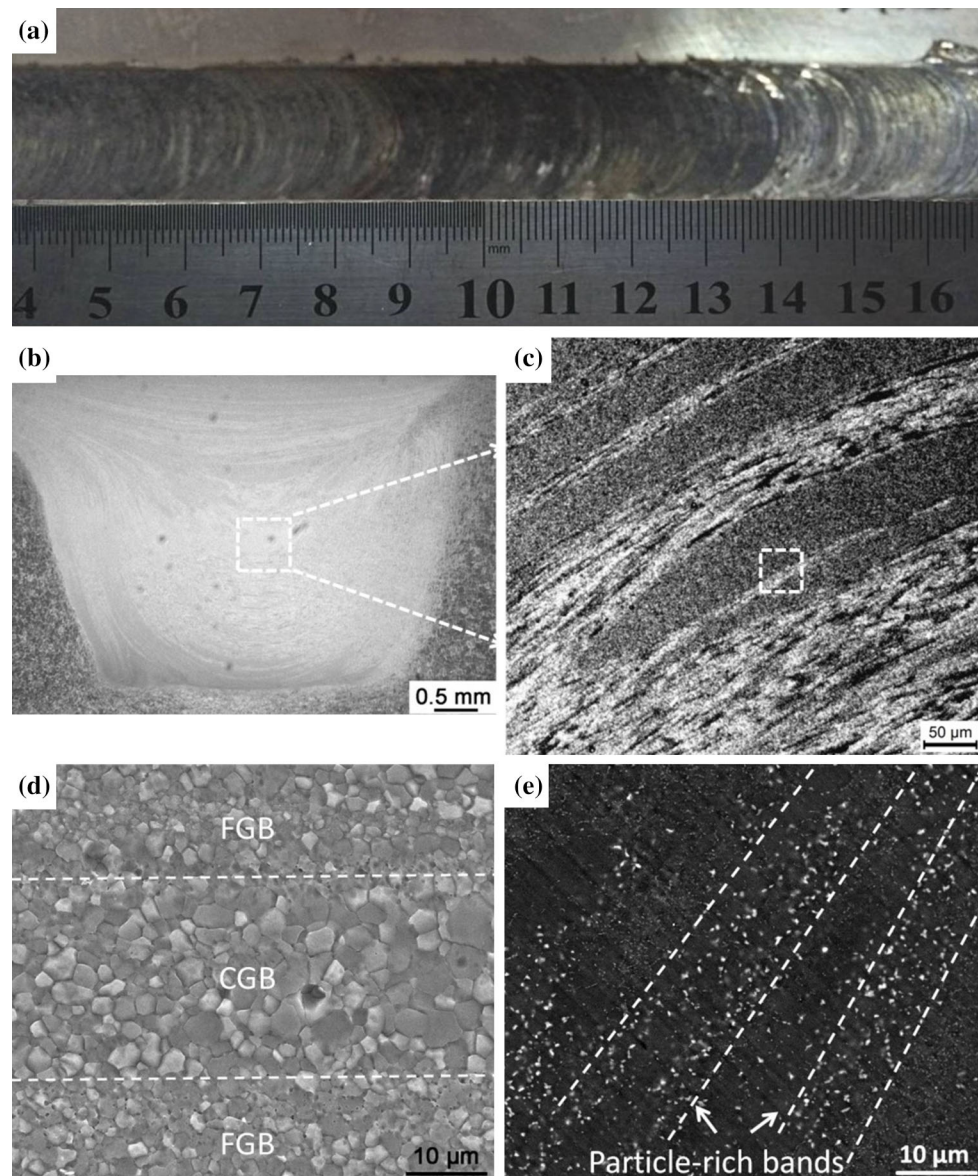After aging at 150 °C × 54 h and 180 °C × 30 h, the strengths are further increased at the expense of

Figure 3 **a** Image of surface appearance of processed region; **b** Cross section macrograph of FSP specimen; **c** Optical microstructure of the center region in SZ; **d** SEM image showing the grain band structure in SZ; **e** BSE image showing the particle-rich bands in SZ.

elongations. For comparison, after T5 treatment (aging at 250 °C × 16 h), the UTS, YS, and elongation of hot-rolled wrought WE43 alloy are about 270 MPa, 230 MPa, and 7 %, respectively [30]. It indicates that FSP + aging is an effective method to improve mechanical properties of Mg–Y–Nd alloy. Compared to Kumar's research [7], although the strengths of FSP and peak-aged specimens are close to each other, much lower elongations are obtained in our study. Different from the hot-rolled Mg–Y–Nd alloy in Kumar's work, the cast BM in our study is composed

of coarse α-Mg grains and large second phases (Fig. 2). As a result, banded structures are formed in our material after FSP (Fig. 3), which is considered to be the main reason for its low ductility. The effect of banded structures for the poor elongations will be discussed in Sect. 4.2.

Microstructure characteristics of peak-aged specimens

In order to assess the influence of grain size on the mechanical properties of peak-aged specimens,

optical microstructures of the FSP + 150 °C and FSP + 180 °C specimens are shown in Fig. 8. It can be seen that the average grain sizes at peak-aged conditions are almost the same as the FSP specimens. Therefore, in this study, aging treatment has no significant effect on the grain sizes, indicating the high structure stability of FSP Mg–Y–Nd alloy. It is well accepted that the formation of thermal stable second-phase particles is beneficial for the good heat-resistance of Mg–RE alloys [18, 31]. As shown in Fig. 3e, small second-phase particles are distributed in FSP specimen, which play a crucial role on the structure stability during aging treatment.
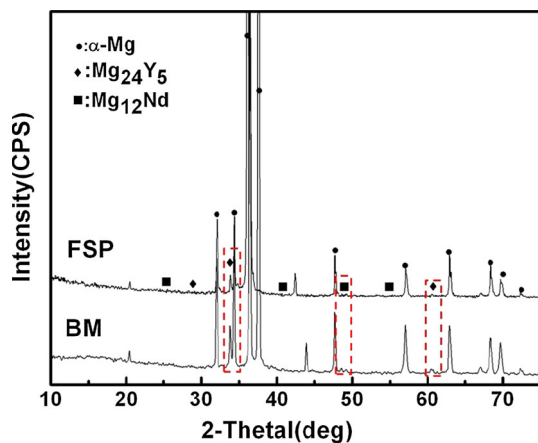
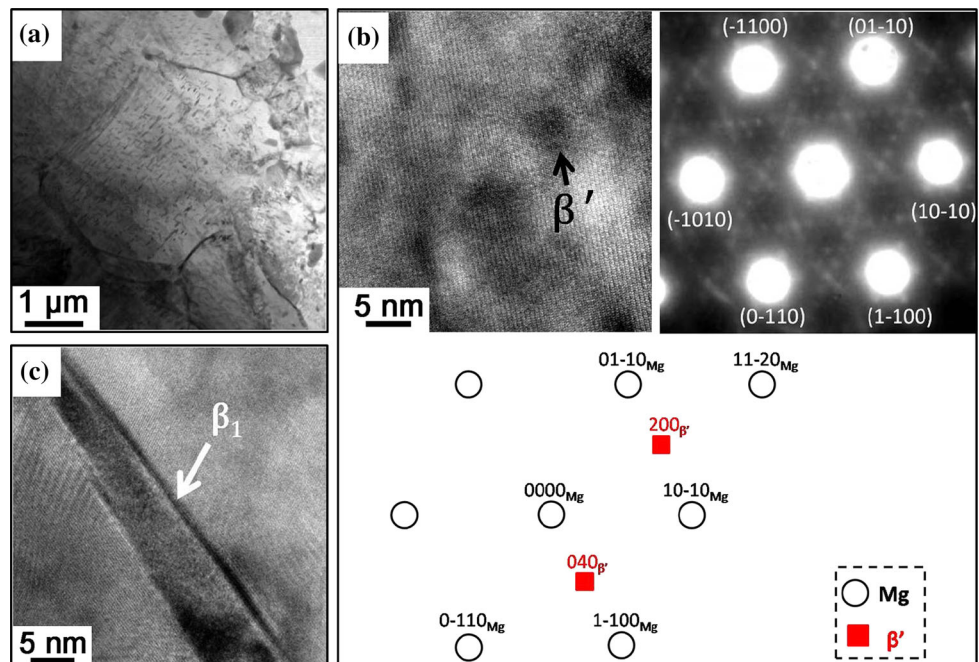Figure 4 X-ray diffraction patterns of BM and FSP specimens.

Figure 9 shows the BSE images of FSP + 150 °C and FSP + 180 °C specimens. After aging treatment, the particle-rich bands are still retained. For FSP + 150 °C specimens, by means of SEM observation, the quantity and distribution of small particles ($Mg_{12}Nd$ and $Mg_{24}Y_5$) have no significant change compared with FSP specimen (Fig. 9a). However, after aging at 180 °C × 30 h, small particles and fine precipitates are both examined (Fig. 9b). As shown by the high-magnification image inserted in Fig. 9b, the plate-shaped precipitates are observed.

The fine precipitates in FSP and peak-aged specimens are examined by TEM. Figure 10a shows that the small particles ($Mg_{12}Nd$ and $Mg_{24}Y_5$) and the plate-shaped β_1 precipitates coexist in FSP specimen. After aging at 150 °C × 54 h, as shown in Fig. 10b, the quantity of β_1 precipitates is similar with the FSP specimens. However, the magnified view reveals that finer precipitates are significantly increased, as shown by the high-magnification image inserted in Fig. 10b. The corresponding SADP along the $[0001]_{Mg}$ orientation shows that the extra spots located at $1/2(1-100)_{Mg}$, indicating the formation of β'' precipitates, with a double hexagonal cell ($a = 2a_{Mg} = 0.64$ nm and $c = c_{Mg} = 0.521$ nm). It is reported that the dominated precipitates in WE43 alloy are β'' when aged at 150 °C [18–20]. Similarly, in this study, amounts of β'' precipitates are shown in α-Mg grains after aging at 150 °C. Figure 10c shows the TEM

Figure 5 a TEM image of FSP specimen; b HREM image of β′ precipitates and the corresponding SADP and the schematic diagram illustrating the indexing of the diffraction pattern; c HREM image of β₁ precipitates. Electron beam is parallel to $[0001]_{Mg}$.
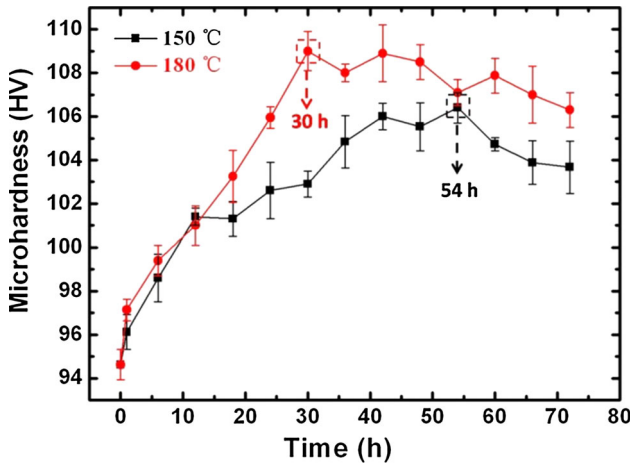
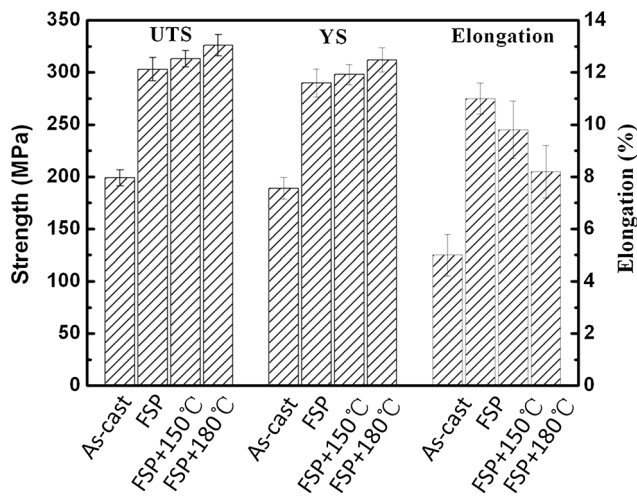**Figure 6** Age hardening curves of FSP specimens aged at 150 and 180 °C.

Figure 7 Histogram showing tensile properties of experimental specimens.

image of FSP + 180 °C specimen. It is clear that the β_1 precipitates are remarkably increased compared with the FSP specimen. The β_1 precipitates are preferentially nucleated on microstructure defects [22, 32] or nucleated in conjunction with globular β' precipitates [17]. Dislocations and β' precipitates in FSP specimens are in favor of the formation of β_1 precipitates when aging at 180 °C. Therefore, precipitation strengthening is the main reason for the strengths improvement after aging treatment; the high strengths obtained by aging at 150 °C × 54 h and 180 °C × 30 h are attributed to the vast of β'' and β_1 precipitates, respectively.

Discussion

Dissolution and precipitation behavior of Mg–Y–Nd cast alloy during FSP

Figure 11a shows an enlarged TEM image of coarse $Mg_{12}Nd$ phase in BM. It can be observed that α-Mg and $Mg_{12}Nd$ phases are mingled with each other in the intergranular region. The sufficient contact area between matrix and second phases can afford more diffusion channels and short diffusion distance, which are beneficial for the dissolution behavior during FSP. As shown in Fig. 11b, coarse α-Mg grains are greatly refined after processing. The large second phases ($Mg_{12}Nd$ and $Mg_{24}Y_5$) in BM are transformed into small particles or dissolved into the matrix. Moreover, dislocations are introduced by SPD during FSP, which allows the occurrence of pipe diffusion [33]. It is reported that the pipe diffusion rate is at least 1000 times higher than the bulk diffusion for Mg [34]. Therefore, the comprehensive effect of short diffusion distance and pipe diffusion can significantly accelerate diffusion rate during FSP.

Figure 12 shows the curve of thermal histories during FSP, and the detailed data are shown by the inserted table. As shown in Fig. 12, the temperature increases with the decreasing distance between pin and measured position, and the peak temperature during processing is 346.2 °C. One thing should be pointed out that the measured position is just set close to SZ as possible, so the measured temperatures may slightly lower than the real values.

The precipitates in aged samples of Mg–Y–Nd alloys have been characterized in several studies. For the aging temperature of 250 °C, the globular and platelet precipitates (β') are formed firstly, and the β_1 precipitates are identified after aging for 16 h [18]. When the aging temperature is increased to 300 °C, the β_1 precipitates are in situ transformed directly on the {11–20}$_{Mg}$ planes after 9 min aging [20]. With the temperature increasing, β' and β_1 precipitates are readier to be formed. According to the thermal history results (Fig. 12), FSP can provide high temperature for the formation of β' and the transformation of β_1 precipitates. Similarly, FSP results in the elimination of β-Mg$_3$RE eutectics and the formation of long–period stacking ordered phase in Mg–Gd–Y–Zn–Zr cast alloy [35]. One phenomenon should be noticed that the rate of precipitation during FSP is much quicker than that of aging under the static conditions.
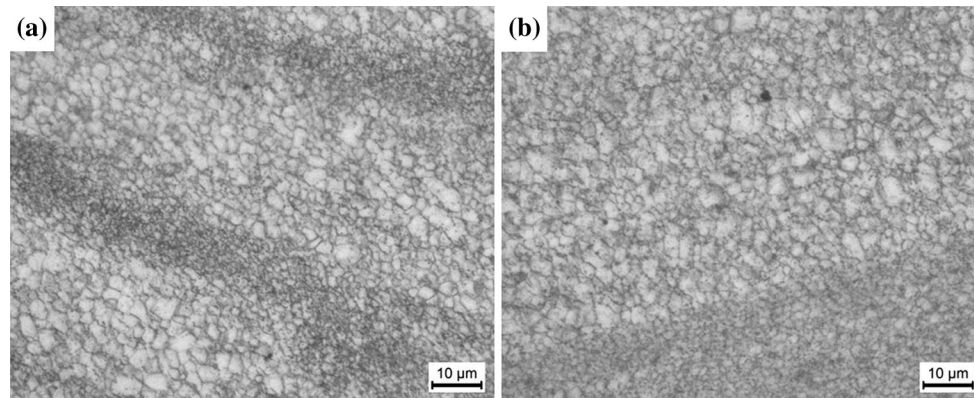
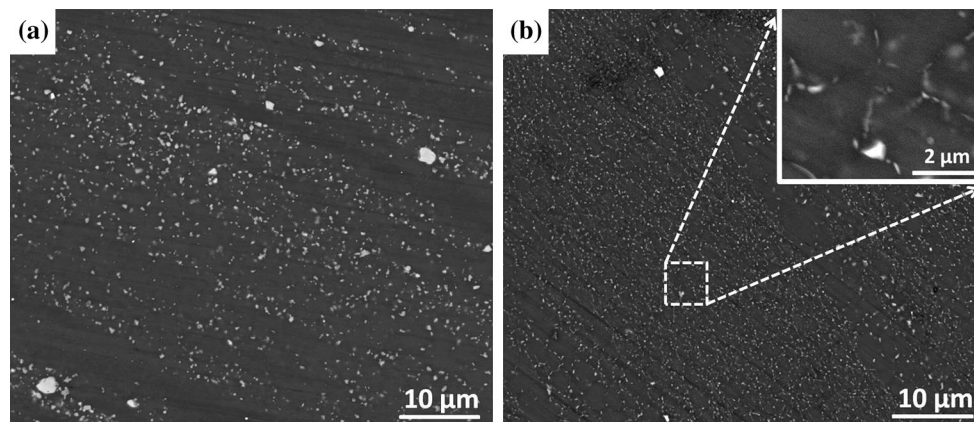**Figure 8** Optical images showing the grains of: **a** FSP + 150 °C; **b** FSP + 180 °C.

Figure 9 BSE images showing the particles of: **a** FSP + 150 °C; **b** FSP + 180 °C.

For instance, β_1 precipitates are formed within 15.6 s above 300 °C during FSP, but 540 s are needed for artificial aging at 300 °C [20]. Two reasons may be responsible for the quick precipitation behavior during FSP: (I) precipitation with the help of pipe diffusion through dislocations; (II) local supersaturated matrix can afford enough solutes in a short time. Further investigations are needed to reveal the precipitation mechanism during FSP.

Failure mechanism of experimental specimens

It is well accepted that the combined mechanical properties of Mg–RE cast alloys can be significantly improved by the heat treatment such as solution + aging [36–39]. Due to the dissolution behavior during FSP, the strengths of FSPed Mg–Zn–Nd–Gd–Zr [28] and Mg–Gd–Y–Zr [6, 29] cast alloys are also remarkably increased after subsequent artificial aging

without solution treatment. In Yang's research [29], the size and density of precipitates (β') are almost the same in cast-T6 and FSP-T5 Mg–Gd–Y–Zr alloy, and the discontinuous precipitates together with narrow precipitates-free zones (PFZs) are commonly observed in the cast-T6 specimen but seldom detected in the FSP-T5 specimen. Since the PFZs are softer than the precipitation hardened matrix, micro-voids are easily nucleated in the PFZs during deformation, resulting in the occurrence of intergranular fracture of the alloy [40, 41]. According to these reports, the FSP Mg–Y–Nd cast alloy is directly subjected to artificial aging without solution treatment in this study. According to Figs. 6 and 7, the hardness and strength of the peak-aged specimen are improved compared to the FSP alloy. However, the ductilities of the peak-aged specimen decrease to some extent. The fracture behaviors of the FSP and peak-aged specimens are examined to reveal the relationship between the microstructures and the mechanical behaviors in this section.

Figure 10 TEM images of:
a FSP specimen;
b FSP + 150 °C specimen and the corresponding SADP and the schematic diagram illustrating the indexing of the diffraction pattern;
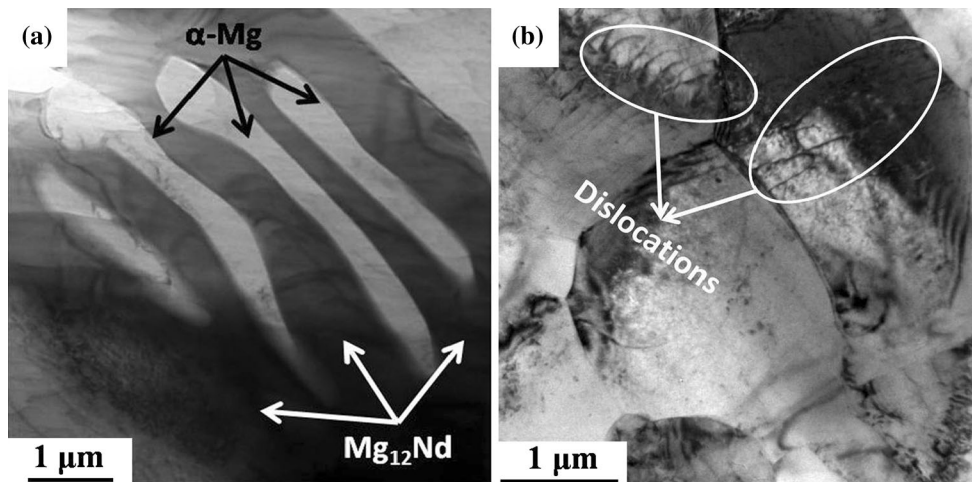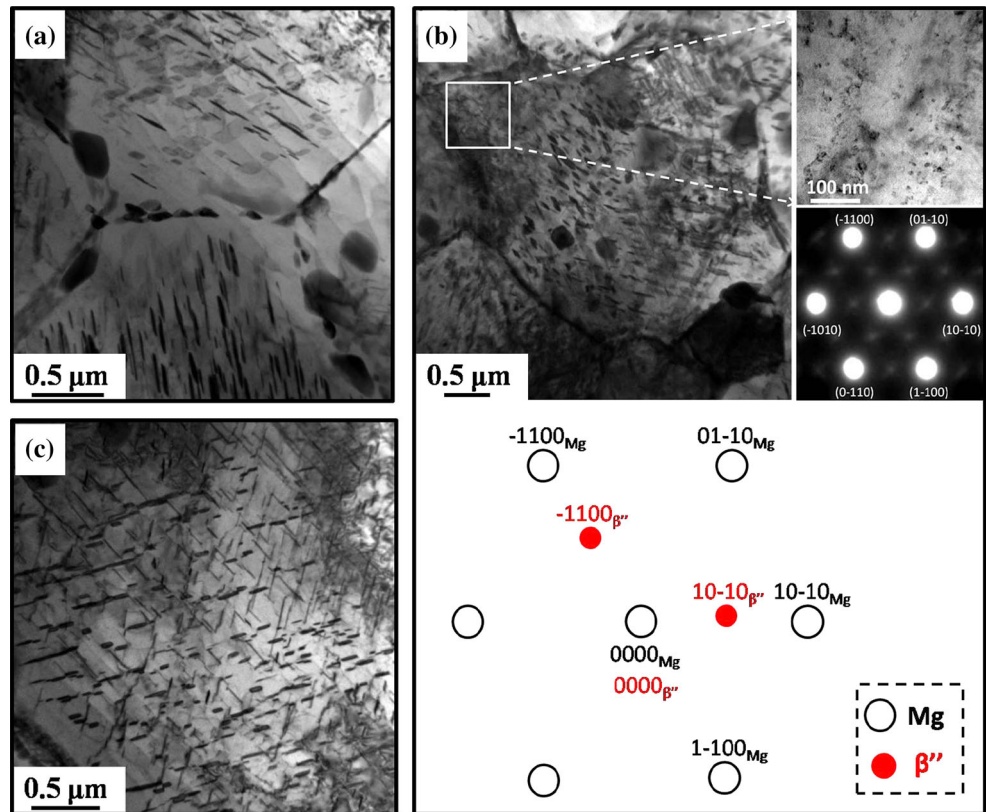**c** FSP + 180 °C specimen. Electron beam is parallel to $[0001]_{Mg}$.

Figure 11 TEM images of **a** BM and **b** FSP specimens.

Figure 13 reveals the tensile fracture appearance of tested specimens. Along with the normal direction (ND), the onion rings (correspond to the CGBs and FGBs mentioned above) are observed in the PD of the FSP and peak-aged specimens. For FSP specimen, cracks tend to spread along with the onion rings (Fig. 13a). However, the fracture paths do not continuously follow the trace of band structures for peak-aged specimens; some bulges can be seen at the edge of cracks, as marked in Fig. 13b, c with circles. It indicates that some micro-cracks propagate perpendicular to the onion rings during the fracture process.

In order to reveal the spread paths of micro-cracks in the fractured specimens, optical images of the PD near fracture surface are shown in Fig. 14. In FSP specimen, micro-cracks are nucleated between FGBs
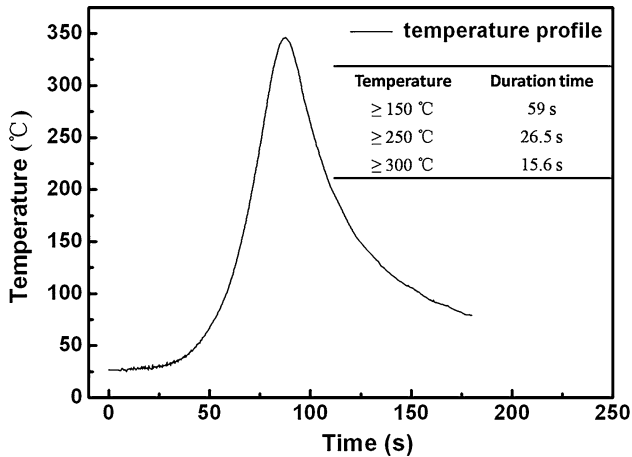
Figure 12 Thermal histories curve during FSP.

and CGBs (case I in Fig. 14a) or propagated in CGBs (case II in Fig. 14a). However, for the fractured specimen of FSP + 180 °C, besides the case I and II,

micro-cracks also appear in the FGBs (case III in Fig. 14b), indicating the additional fracture paths after aging. According to the TEM observation (Fig. 10), lots of β_1 precipitates appear after aging at 180 °C × 30 h. Since cracks are easily formed in the precipitate-rich regions, more crack nucleation sites are provided. This is the main reason that the elongations of aged specimens are decreased compared with the FSP specimen.

Figure 15 gives the TD fracture morphologies of fractured specimens. Limited tear ridges and abundant cleavage facets can be seen on the fracture surface of as-cast specimen (Fig. 15a), indicating the dominated failure mode is quasi-cleavage fracture [12]. Figure 15b shows the smooth fracture surface of FSP specimen, which is attributed to the cracks in FSP specimen which are tended to spread along with the band structures. However, the fracture surfaces of
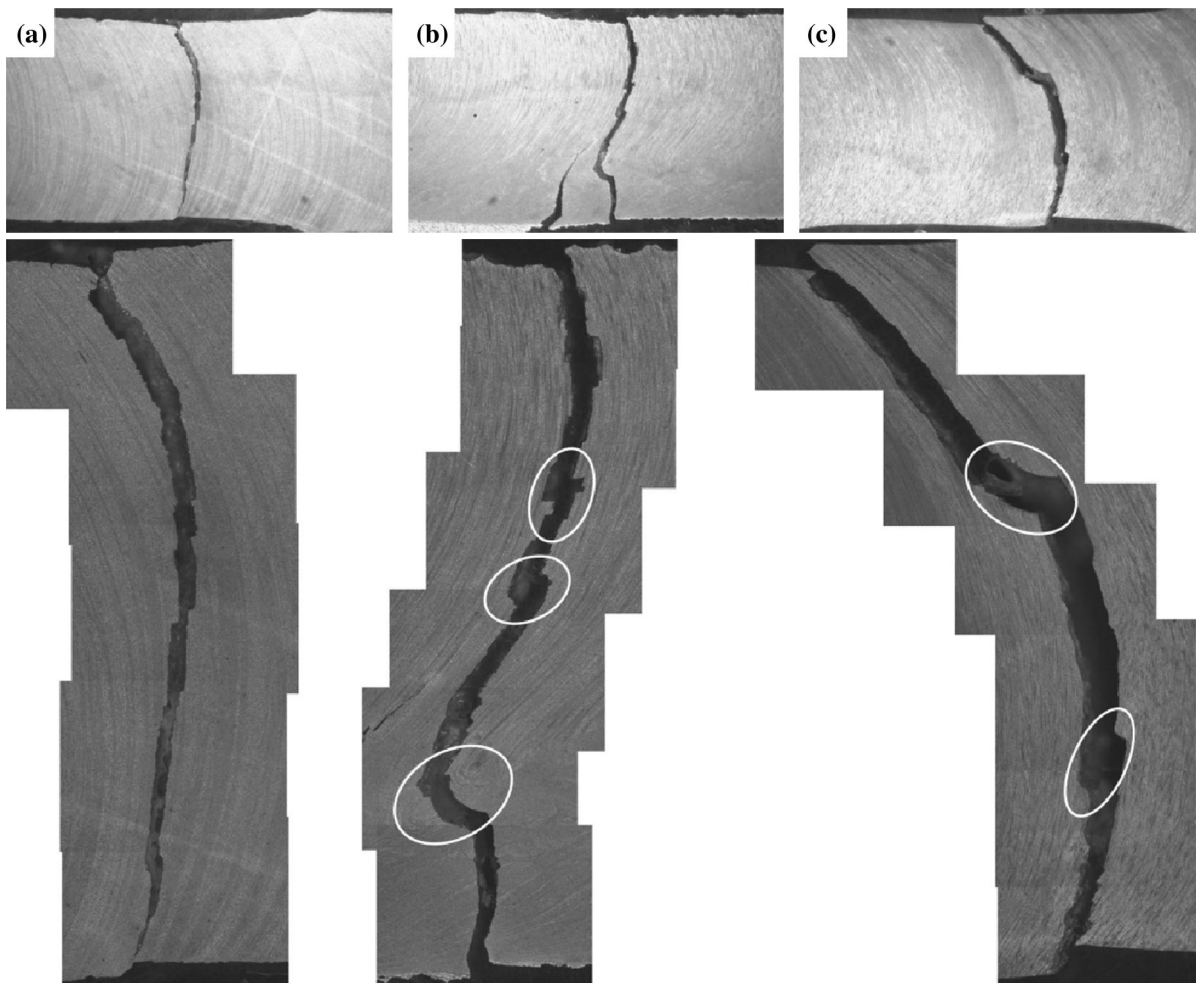

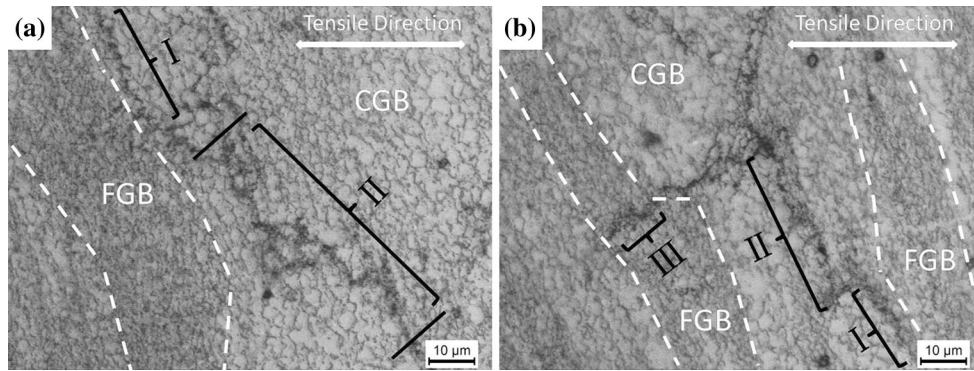Figure 13 Tensile fracture appearance of specimens: **a** FSP; **b** FSP + 150 °C; **c** FSP + 180 °C.

Figure 14 Micro-crack growth paths: **a** FSP specimen; **b** specimen aged at 180 °C × 30 h.
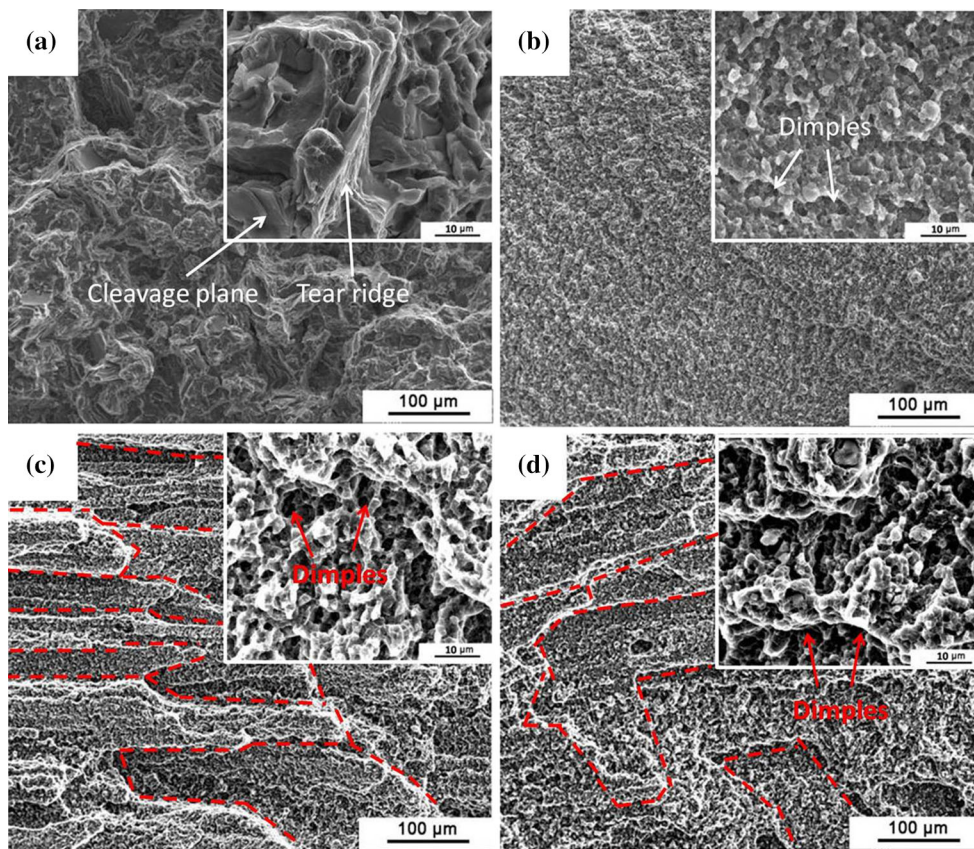

Figure 15 SEM images of tensile fracture surfaces: **a** As-cast; **b** FSP; **c** FSP + 150 °C; **d** FSP + 180 °C.

FSP + 150 °C and FSP + 180 °C specimens reveal a step type of profile, as the dotted lines marked in Fig. 15c, d, which correspond to the additional fracture paths in peak-aged specimens. The magnified views reveal that dimples and small cleavage facets are exhibited on the fracture surfaces of FSP and peak-aged specimens (as shown the inserted images in Fig. 15b–d), indicating that the failure mechanisms of FSP and peak-aged specimens are all mixed ductile-brittle fracture mode [42, 43].

The influence of particle-rich bands on elongation of FSP specimen is examined by BSE observation. As shown in Fig. 16a, dimples, cleavage facets, and particle-rich bands are exhibited on the fracture surface of FSP specimen. Plastic deformation is not uniform between particles/matrix and FGBs/CGBs,

Figure 16 a BSE image showing the tensile fracture surface of FSP specimen; **b** Schematic diagram of the fracture path in FSP specimen.
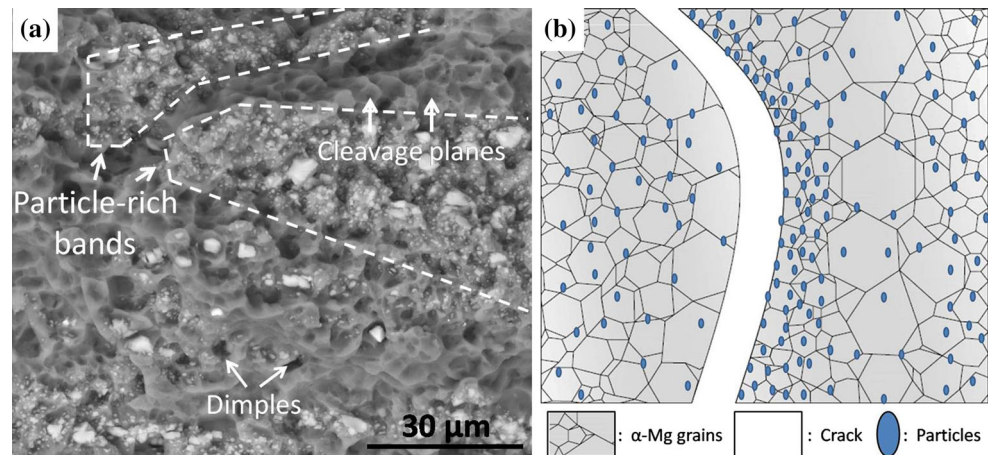
resulting in the stress concentration in these areas [44–47]. Therefore, cracks tend to nucleate or spread along with the band structures, as illustrated in Fig. 16b. This is the main reason for the limited improvement of elongations in the FSP and peak-aged specimens, although microstructures of these materials are refined greatly compared to the as-cast alloy.

Conclusions

The following conclusions can be drawn from this study:

1. Microstructure of the as-cast Mg–Y–Nd alloy is refined greatly after FSP; the average grain size of FSP specimen is ~ 2.7 μm.
2. The peak temperature during FSP is about 346 °C. Due to the heat input, β' and β_1 precipitates are formed during cooling.
3. The UTS, YS, and elongation of FSP specimen are 303 MPa, 290 MPa, and 11 %, respectively, which are much higher than those of as-cast specimen. After aging at 150 °C × 54 h and 180 °C × 30 h, the strengths of FSP specimen are increased, which is mainly attributed to the presence of β'' and β_1 precipitates, respectively. Meanwhile, the elongations are both decreased slightly after aging treatment.
4. In FSP specimen, micro-cracks are nucleated between FGBs and CGBs, propagated in CGBs, while the micro-cracks appear in the FGBs after aging treatment, providing the additional fracture paths. The failure mechanisms of FSP and peak-aged specimens are all mixed ductile-brittle fracture mode.

References

[1] Mishra RS, Mahoney MW, McFadden SX, Mara NA, Mukherjee AK (1999) High strain rate superplasticity in a friction stir processed 7075 Al alloy. Scr Mater 42:163–168

[2] Mishra RS, Ma ZY (2005) Friction stir welding and processing. Mater Sci Eng R 50:1–78

[3] Ma ZY (2008) Friction stir processing technology: a review. Metall Mater Trans A 39:642–658

[4] Charit I, Mishra RS (2005) Low temperature superplasticity in a friction-stir-processed ultrafine grained Al–Zn–Mg–Sc. Acta Mater 53:4211–4233

[5] Yang Q, Xiao BL, Ma ZY, Chen RS (2011) Achieving high strain rate superplasticity in Mg–Zn–Y–Zr alloy produced by friction stir processing. Scr Mater 65:335–338

[6] Xiao BL, Yang Q, Yang J, Wang WG, Xie GM, Ma ZY (2011) Enhanced mechanical properties of Mg–Gd–Y–Zr casting via friction stir processing. J Alloys Compd 509:2879–2884

[7] Kumar N, Dendge N, Banerjee R, Mishra RS (2014) Effect of microstructure on the uniaxial tensile deformation behavior of Mg–4Y–3RE alloy. Mater Sci Eng A 590:116–131

[8] Ke LM, Huang CP, Xing L, Huang KH (2010) Al–Ni intermetallic composites produced in situ by friction stir processing. J Alloys Compd 503:494–499

[9] Fonda RW, Bingert JF (2006) Precipitation and grain refinement in a 2195 Al friction stir weld. Metall Mater Trans A 37:3593–3604

[10] Sato YS, Kokawa H, Enomoto M, Jogan S (1999) Microstructural evolution of 6063 aluminum during friction-stir welding. Metall Mater Trans A 30:2429–2437

[11] Panigrahi SK, Yuan W, Mishra RS, DeLorme R, Davis B, Howell RA, Cho K (2011) A study on the combined effect of forging and aging in Mg–Y–RE alloy. Mater Sci Eng A 530:28–35

[12] Su Z, Liu C, Wan Y (2013) Microstructures and mechanical properties of high performance Mg–4Y–2.4Nd–0.2Zn–0.4Zr alloy. Mater Des 45:466–472

[13] Kumar N, Choudhuri D, Banerjee R, Mishra RS (2015) Strength and ductility optimization of Mg–Y–Nd–Zr alloy by microstructural design. Int J Plast 68:77–97

[14] Cao GH, Zhang DT, Zhang W, Qiu C (2015) Microstructure evolution and mechanical properties of Mg–Nd–Y alloy in different friction stir processing conditions. J Alloys Compd 636:12–19

[15] Barucca G, Ferragut R, Fiori F, Lussana D, Mengucci P, Moia F, Riontino G (2011) Formation and evolution of the hardening precipitates in a Mg–Y–Nd alloy. Acta Mater 59:4151–4158

[16] Nie JF, Muddle BC (1999) Precipitation in magnesium alloy WE54 during isothermal ageing at 250 °C. Scr Mater 40:1089–1094

[17] Nie JF, Muddle BC (2000) Characterisation of strengthening precipitate phases in a Mg–Y–Nd alloy. Acta Mater 48:1691–1703

[18] Antion C, Donnadieu P, Perrard F, Deschamps A, Tassin C, Pisch A (2003) Hardening precipitation in a Mg–4Y–3RE alloy. Acta Mater 51:5335–5348

[19] Mengucci P, Barucca G, Riontino G, Lussana D, Massazza M, Ferragut R, Aly EH (2008) Structure evolution of a WE43Mg alloy submitted to different thermal treatments. Mater Sci Eng A 479:37–44

[20] Apps PJ, Karimzadeh H, King JF, Lorimer GW (2003) Precipitation reactions in magnesium–rare earth alloys containing yttrium, gadolinium or dysprosium. Scr Mater 48:1023–1028

[21] Xu Z, Weyland M, Nie JF (2014) On the strain accommodation of β_1 precipitates in magnesium alloy WE54. Acta Mater 75:122–133

[22] Nie JF (2012) Precipitation and hardening in magnesium alloys. Metall Mater Trans A 43:3891–3939

[23] Nie JF, Wilson NC, Zhu YM, Xu Z (2016) Solute clusters and GP zones in binary Mg–RE alloys. Acta Mater 106:260–271

[24] Choudhuri D, Dendge N, Nag S, Meher S, Alam T, Gibson MA, Banerjee R (2014) Homogeneous and heterogeneous precipitation mechanisms in a binary Mg-Nd alloy. J Mater Sci 49:6986–7003. doi:10.1007/s10853-014-8404-z

[25] Chai F, Zhang DT, Li YY, Zhang W (2015) Microstructure evolution and mechanical properties of a submerged friction-stir-processed AZ91 magnesium alloy. J Mater Sci 50:3212–3225. doi:10.1007/s10853-015-8887-2

[26] Cao GH, Zhang DT, Chai F, Zhang WW, Qiu C (2015) Superplastic behavior and microstructure evolution of a fine-grained Mg–Y–Nd alloy processed by submerged friction stir processing. Mater Sci Eng A 642:157–166

[27] Mahoney MW, Rhodes CG, Flintoff JG, Spurling RA, Bingel WH (1998) Properties of friction-stir-welded 7075 T651 aluminum. Metall Mater Trans A 29:1955–1964

[28] Freeney TA, Mishra RS (2010) Effect of friction stir processing on microstructure and mechanical properties of a cast-magnesium–rare earth alloy. Metall Mater Trans A 41:73–84

[29] Yang Q, Xiao BL, Ma ZY (2012) Influence of process parameters on microstructure and mechanical properties of friction-stir-processed Mg–Gd–Y–Zr Casting. Metall Mater Trans A 43:2094–2109

[30] Yu K, Li WX, Wang RC, Wang B, Li C (2008) Effect of T5 and T6 tempers on a hot-rolled WE43 magnesium alloy. Mater Trans 49:1818–1821

[31] Riontino G, Massazza M, Lussana D, Mengucci P, Barucca G, Ferragut R (2008) A novel thermal treatment on a Mg–4.2Y–2.3Nd–0.6Zr (WE43) alloy. Mater Sci Eng A 494:445–448

[32] Choudhuri D, Meher S, Nag S, Dendge N, Hwang J, Banerjee R (2013) Evolution of a honeycomb network of precipitates in a hot-rolled commercial Mg–Y–Nd–Zr alloy. Philos Magn Lett 93:395–404

[33] Ma ZY, Pilchak AL, Juhas MC, Williams JC (2008) Microstructural refinement and property enhancement of cast light alloys via friction stir processing. Scr Mater 58:361–366

[34] Frost HJ, Ashby MF (1982) Deformation mechanism Map. Pergamon Press, Oxford

[35] Yang Q, Xiao BL, Wang D, Zheng MY, Ma ZY (2015) Study on distribution of long-period stacking ordered phase in Mg–Gd–Y–Zn–Zr alloy using friction stir processing. Mater Sci Eng A 626:275–285

[36] Ning ZL, Yi JY, Qian M, Sun HC, Cao FY, Liu HH, Sun JF (2014) Microstructure and elevated temperature mechanical and creep properties of Mg–4Y–3Nd–0.5Zr alloy in the product form of a large structural casting. Mater Des 60:218–225

[37] Liu SJ, Yang GY, Luo SF, Jie WQ (2015) Microstructure and mechanical properties of sand mold cast Mg–4.58Zn–2.6Gd–0.18Zr magnesium alloy after different heat treatments. J Alloys Compd 644:846–853

[38] Zhang Y, Wu YJ, Peng LM, Fu PH, Huang F, Ding WJ (2014) Microstructure evolution and mechanical properties of an ultra-high strength casting Mg–15.6Gd–1.8Ag–0.4Zr alloy. J Alloys Compd 615:703–711

[39] Kang YH, Yan H, Chen RS (2015) Effects of heat treatment on the precipitates and mechanical properties of sand-cast Mg–4Y–2.3Nd–1Gd–0.6Zr magnesium alloy. Mater Sci Eng A 645:361–368

[40] Zheng KY, Dong J, Zeng XQ, Ding WJ (2008) Effect of precipitation aging on the fracture behavior of Mg–11Gd–2Nd–0.4Zr cast alloy. Mater Charact. 59:857–862

[41] Zheng KY, Dong J, Zeng XQ, Ding WJ (2008) Precipitation and its effect on the mechanical properties of a cast Mg–Gd–Nd–Zr alloy. Mater Sci Eng A 489:44–54

[42] Shi XH, Zeng WD, Shi CL, Wang HJ, Jia ZQ (2015) The fracture toughness and its prediction model for Ti–5Al–5Mo–5V–1Cr–1Fe titanium alloy with basket–weave microstructure. J Alloys Compd 632:748–755

[43] Kong DJ, Liu H, Wang JC (2015) Effects of micro arc oxidation on fatigue limits and fracture morphologies of 7475 high strength aluminum alloy. J Alloys Compd 650:393–398

[44] Lu YZ, Wang QD, Ding WJ, Zeng XQ, Zhu YP (2000) Fracture behavior of AZ91 magnesium alloy. Mater Lett 44:265–268

[45] Yang J, Ni DR, Wang D, Xiao BL, Ma ZY (2014) Friction stir welding of as-extruded Mg–Al–Zn alloy with higher Al content. Part I: Formation of banded and line structures. Mater Charact 96:142–150

[46] Uematsu Y, Tokaji K, Fujiwara K, Tozaki Y, Shibata H (2009) Fatigue behaviour of cast magnesium alloy AZ91 microstructurally modified by friction stir processing. Fatigue Fract Eng Mater Struct 32:541–551

[47] Prakash DGL, Regener D (2008) Quantitative characterization of $Mg_{17}Al_{12}$ phase and grain size in HPDC AZ91 magnesium alloy. J Alloys Compd 461:139–146